Direct visualization and 3D reconstruction of conductive filaments in aSiO2 material-based memristive device

Stanislav Slang[a], Bin Gu[b], Bo Zhang[b*], Petr Janicek[a,c], Jhonatan Rodriguez Pereira[a], Tomas Wagner[a,d]

[a]Center of Materials and Nanotechnologies, Faculty of Chemical Technology, University of Pardubice, nam. Cs. Legii 565, Pardubice 530 02, Czech Republic
[b]College of Physics, Hebei Normal University, Shijiazhuang 050024, China
[c]Institute of Applied Physics and Mathematics, Faculty of Chemical Technology, University of Pardubice, Studentska 95, Pardubice 530 02, Czech Republic
[d]Department of General and Inorganic Chemistry, Faculty of Chemical Technology, University of Pardubice, Studentska 573, 532 10 Pardubice, Czech Republic

KEYWORDS conductive filament; memristive device

Abstract Observation of conductive filaments has greatly aided the development of theoretical models of memristive devices. In this work, we visualized the morphology of conductive filaments in a Cu/Cu-doped SiO_2/W device employing a focused ion beam (FIB) as a milling technique. The SEM images taken from the device after 150 DC sweep cycles showed that Joule heat played a vital role in determining the morphology of a conductive filament, where the vaporization of the conductive filament results in the creation of defects, including particles, voids, and cavities. The competition between the formation and vaporization of conductive filaments generally induces remarkable current fluctuations. Since Cu-doped SiO_2 was utilized as the electrolyte, the vapors also exfoliated adjacent single layers. FIB milling proceeded in top-down and front-back modes; thus, a 3D model of conductive filaments and defects was constructed based on a series of FIB-SEM images. This methodology is promising for a future failure analysis of memristive devices.

INTRODUCTION

Memristive devices, emerging as a new generation of memory devices, are electric resistive switches that have been studied since the early 1970s[1,2]. The electrochemical metallization mechanism (ECM), which includes the growth and rupture of conductive filaments, has been employed to explain the resistive switching phenomena in Cu- or Ag-doped oxides or chalcogenide materials, such as Ag_2S, CuS, and Ag-GeS_x. Cu-GeS_x, etc.[3–6]. The resistance changes during the microscale process in 3 steps: oxidation of the anion electrolyte, migration of ions, and reduction of ions. In the RESET process, Joule heat assists the dissolution of conductive filaments in the thinnest region, which has a high electric current density[7]. Regardless of whether the ECM model or other models are described, the cyclic creation and dissolution of conductive filaments are nondestructive process[8]. However, the generation and dissipation of bubbles, reported in the Pt/TiO_2/Pt device, suggest that the electrical reaction has impacted the devices[9].

Since the conductive filaments described in the ECM generally consist of Ag or Cu, various methods have been published to determine the morphology of conductive filaments[10–12]. For example, the dynamic growth of Ag conductive filaments was studied using SEM, in which a dendrite morphology was observed[7]. In situ TEM images of conductive filaments were also obtained for the Pr-Ir/CuGeTe/Cu and Cu/ZrO_2/Pt devices[12,13]. Furthermore, computer simulations based on Monte Carlo analysis have been widely applied as powerful tools for reconstructing 3D models of conductive filaments, and several physical models have also been published[14,15]. However, the understanding of conductive filaments is still limited, especially from a 3D view.

2D materials have long been used as electrolytes or electrode materials in memristive devices[16,17]. However, the size of fabricated flakes always restricts their application[18]. We invented a method to synthesize amorphous or polycystalline metal, oxide and chalcogenide 2D materials via magnetron sputtering and thermal evaporation[19]. Our method has certain advantages over traditional methods in terms of thickness, material size and compatibility and is promising for use in future electronic devices.

In this paper, we fabricated a memristive device with a W/Cu-doped SiO_2/Cu structure, the surface morphology of which changed after DC sweeps. Further front-back and top-bottom milling revealed that the vaporation of conductive filaments results in microvoids and delamination of 2D SiO_2 monolayers, hence locally switching the resistance of devices to a high-resistivity state. Solid evidence of a current fluctuation in both the SET and RESET processes confirms the contribution of Joule heat. Our findings help to rebuild the missing part of the ECM model.

EXPERIMENT

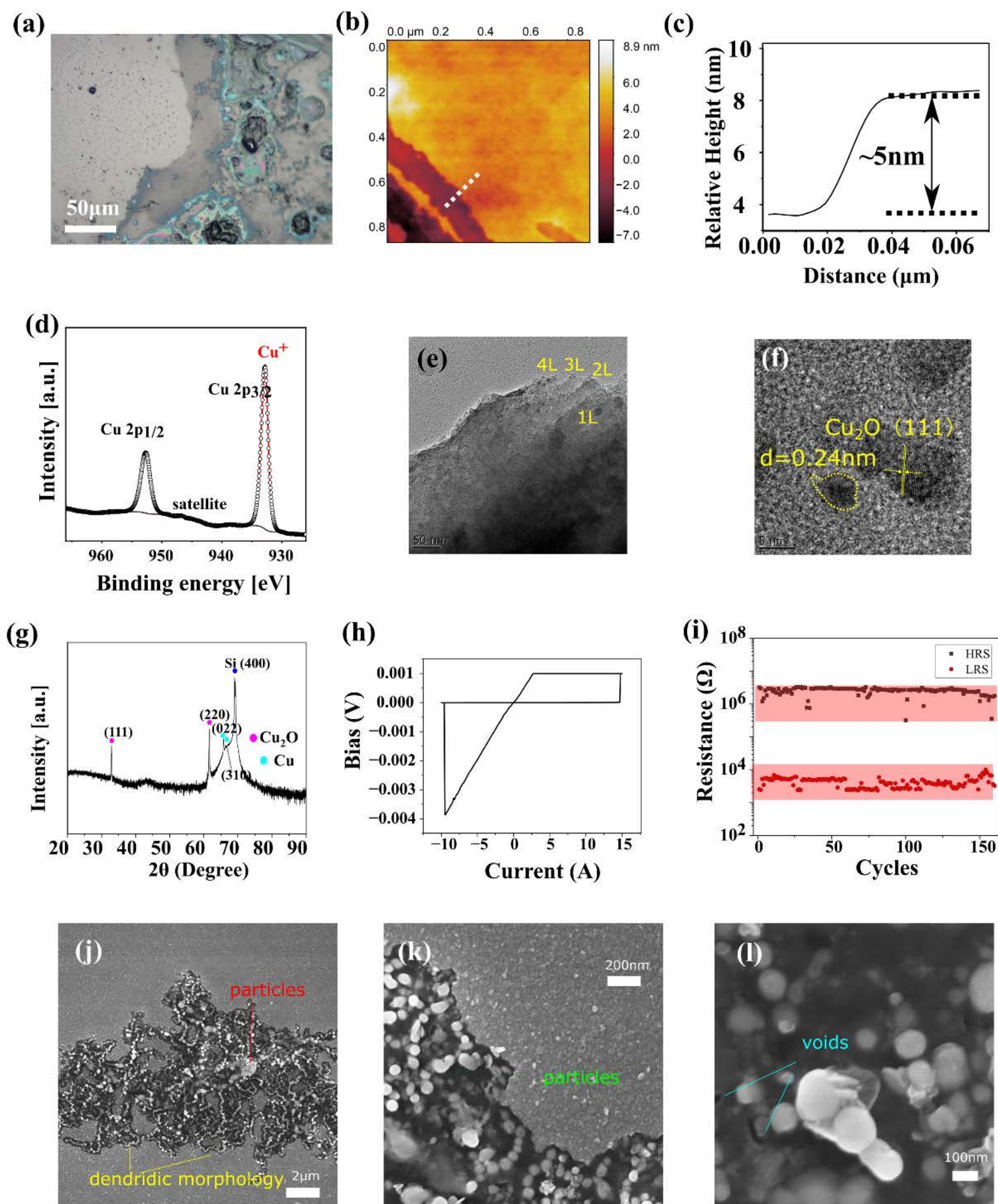

Figure 1 (a) Optical image of a single layer of Cu-doped SiO_2 after exfoliation; (b) surface topography of Cu-doped SiO_2 after exfoliation determined by AFM; (c) profile of steps taken from the dashed line in (b); (d) XPS spectra of Cu-doped SiO_2; (e) TEM images of Cu-doped SiO_2 presenting 4 single layers; (f) HRTEM images of Cu-doped SiO_2 under high resolution; (g) XRD spectra of Cu-doped SiO_2; (h) I-V curve of a Cu/Cu-doped SiO_2/W device with DC sweeping from 15 V to -10 V; (i) endurance of the Cu/Cu-doped SiO_2/W device; (j)-(l) defects, including defects created on the surface of the device after 150 cycles

The Cu-doped SiO_2 was deposited with a composite target that consisted of Cu and

SiO_2 targets assembled vertically, and the composition of the Cu-doped SiO_2 was regulated by the size of the aperture and RF power (see Figure S1). SiO_2 was deposited onto a Si wafer for further AFM, XPS and XRD analyses. Due to the accumulation of internal stress, as-deposited Cu-doped SiO_2 has a multilayer structure with a clear boundary, as shown in the optical image after exfoliation (see Fig. 1 (a)). The rainbow color fringe is the result of light interference, and similar phenomena were observed in our previous paper (ref. 19). The SEM image in Figure S2 shows the existence of an air gap contributing to the light interference. Further AFM studies also confirmed that the height of the step was approximately 5 nm, which is comparable with that of other 2D oxide materials[18]. Thus, in our opinion, multilayered Cu-doped SiO_2 was formed during the cooling of the material after deposition. Moreover, Cu was saturated in SiO_2 and precipitated between the single layers, and the Cu particles were further etched via $FeCl_3$/acetone solution. Thus, the fast vaporization of acetone further helped to delaminate the adjacent single layers. As a consequence, the appearance of the as-deposited Cu-doped SiO_2 changed from colorless to rainbow colors immediately upon contact with the $FeCl_3$/acetone solution. Therefore, single layers were exfoliated, and dispersed into the solution, leaving the terrain with steps (see Fig. 1 (b)-(c)). The valence state of Cu was characterized by XPS, as shown in Figure 1 (d), where the peaks at 955 eV and 952 eV correspond to Cu^{+} and Cu^{0}, respectively, suggesting the coexistence of Cu metallic particles and Cu_2O. The sample for TEM imaging was fabricated with the exfoliation process. The Cu-doped SiO_2 layer was first deposited onto a soluble substrate and subsequently exfoliated in distilled water. Afterwards, drops with dispersed flakes were transferred to the copper grid. Most flakes had a structure with multiple single layers, as shown in Figure 1 (e), from 1 L to 4 L. The Cu_2O particles were deposited inside the amorphous SiO_2 matrix, and the lattice fringe at 0.24 nm was assigned to the (111) planes of Cu_2O (see Fig. 1 (f)). The XRD results suggest the amorphous structure of SiO_2 and the coexistence of Cu and Cu_2O, which agrees with the XPS results, as shown in Figure 1(g). A DC sweep of the Cu/Cu-doped SiO_2/W device was performed by a Keithley 2600, where the topmost Cu electrode and bottom W electrode were connected with positive and negative probes, respectively. I-V curves after more than 150 cycles exhibited good cycle-to-cycle stability with an ~10^2 R_{on}/R_{off} ratio, as shown in Figure 1 (h) and (i). Since the thickness of the device reaches 500 nm, the formation of conductive filaments requires heavy Cu doping, which Cu particles are possibly present at the interface of single layers, to increase the ionic conductivity of the electrolyte layer. Thus, the SET and RESET thresholds are in the range of ~15 V and ~-10 V, respectively, which are clearly higher than those of the other memristive devices described in the literature [20]. After 150 cycles of DC sweeps, we checked the surface electrodes of the device and discovered four different types of defects, including dendritic morphology, particles, and voids, as shown in Figure 1 (j)-(l). In our opinion, these defects might be closely related to the Joule heat during the formation and dissolution of conductive filaments.

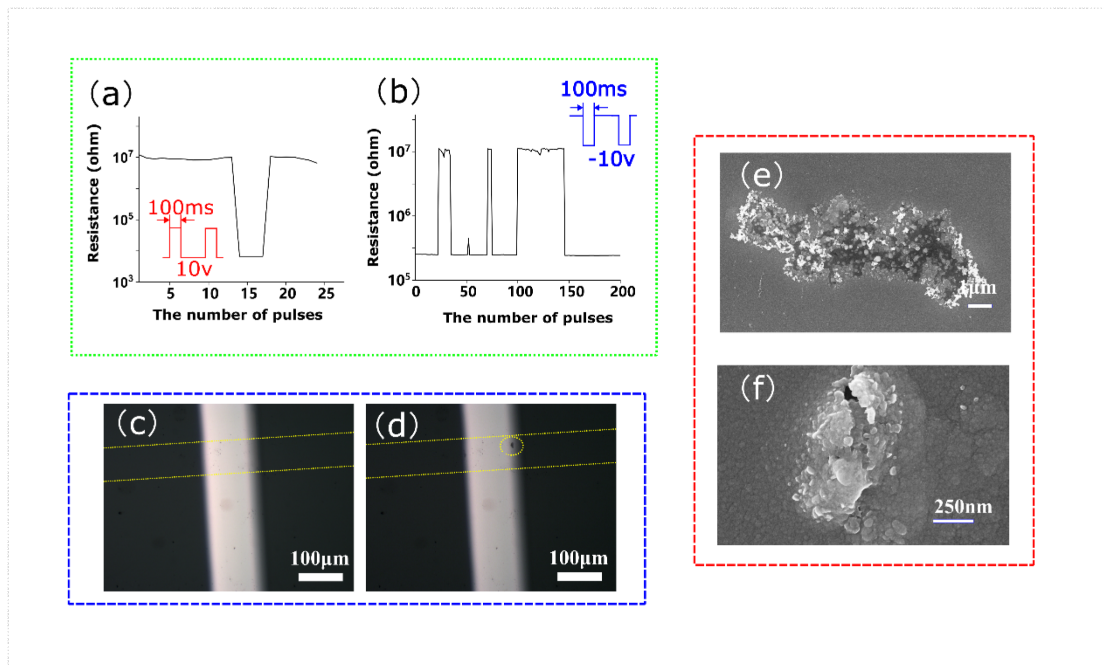

Figure 2 (a) Current fluctuations with successive positive pulses (10 V); (b) current fluctuations with successive positive pulses (-10 V); (c)-(d) surface morphology of devices under SEM after positive DC sweeps (c) and after testing (d), in which the bottom electrode is marked with a dashed yellow line and the defect created in (d) is marked by a yellow dashed circle; (e)-(f) morphology with bubbles (e) and cracks (f) taken from the dashed circle in (d).

As discussed in Figure 1, defects were created during DC sweeping, whereas it is not clear whether these defects were generated during the SET or RESET process. As shown in Figure 1 (j), the size of the defects is large enough to be observed under an optical microscope. Therefore, we designed an experiment in which a series of pulses was applied with bias (10 V, 100 ms and -10 V, 100 ms) to the device. As shown in Figure 2 (a), under successive 10 V pulses, the initial resistance decreased from 10^7 Ω to 10^4 Ω, followed by a recovery of resistance from 10^4 Ω to 10^7 Ω. Similarly, unstable resistances were also found under successive -10 V pulses, as shown in Figure 2 (b). Under an optical microscope (Figure 2 (c)-(d)), a black dot appeared as a dashed yellow circle after the negative pulse measurement. The region in the yellow circle was further observed by SEM (Figure 2(e)), in which the defects, including particles, were presented as damage to the topmost electrode. The crack shown in Figure 2(f) possibly formed because the conductive filament vaporized. In theory, the ions are reduced to conductive filaments during the SET process, resulting in an increase in the current. Moreover, the increased current produces a large amount of Joule heat, helping the dissolution of conductive filaments into the matrix. However, once the Joule heat is large enough, vaporization of the conductive filament occurs, damaging the topmost electrode. As a result, the overall device is temporarily in a high-resistance state until a new conductive filament is built in the other places. Repeating this process leads to a current fluctuation. In conclusion, mild dissolution of filaments is a nondestructive process, whereas vaporization of conductive filaments, accompanied by damage to the

electrode, is a destructive process.

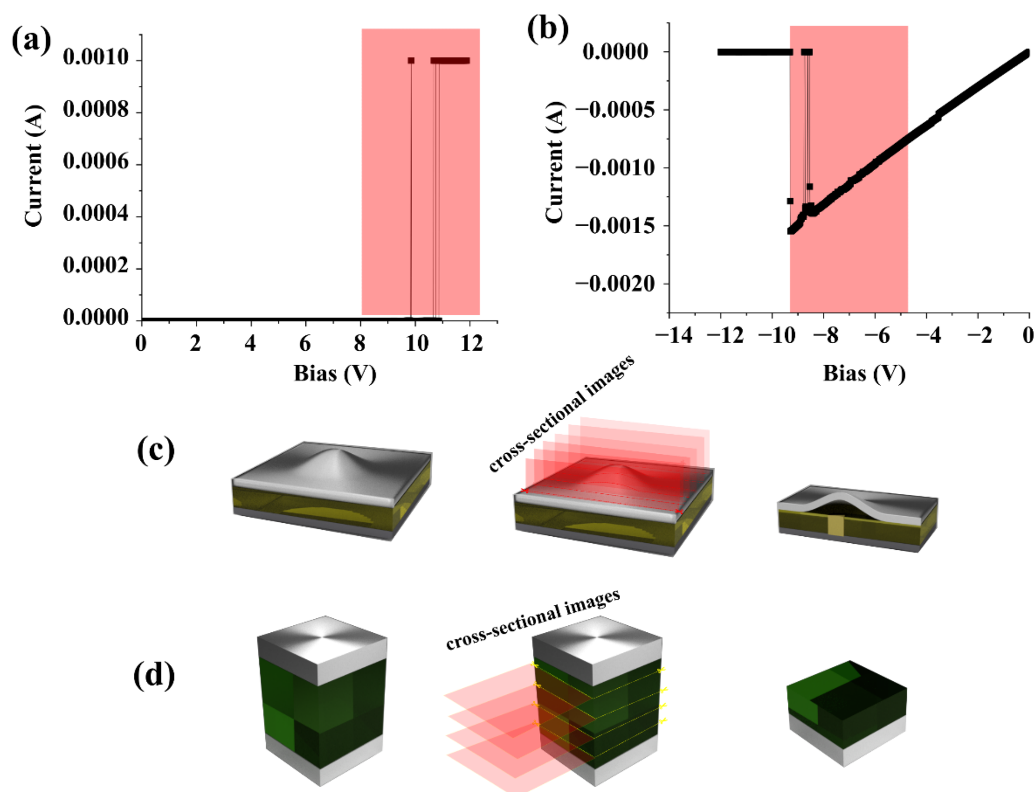

Figure 3 (a) SET process with current fluctuations, marked with red; (b) RESET process with current fluctuations marked with red; (c) method for building the 3D model of the Cu/Cu-doped SiO_2/W device with cross-sectional milling from front to back; (d) method for building the 3D model of the Cu/Cu-doped SiO_2/W device with top-down milling.

To estimate the influence of the DC sweep on defect creation, we performed a positive DC sweep to set the devices in a low-resistance state to study the morphology of the conductive filament, while some devices were consistently subjected to a negative DC sweep to set the device in a high-resistance state to study the partially dissolved conductive filament. As shown in Figure 3 (a), when the bias exceeded 9 V, the current fluctuated, indicating that the resistances flipped between the high-resistance state and low-resistance state, which is in agreement with the results shown in Figure 2. Similarly, the current was in an unstable state once the DC reached -8 V. However, the current fluctuation occurred randomly in some specific cycles, which could be the first cycle or the last few cycles; thus, it is almost impossible to predict when the current

fluctuation would occur. To shed more light on this issue, devices in the SET and RESET states were transferred for FIB milling, and front-back milling and top-down milling were performed as schematically shown in Figure 3 (c) and (d), respectively. In the top-down milling, SEM images were taken after each 10 s, whereas the sputtering rate at different spots could not be precisely controlled. As an alternative solution, front-back milling was performed with a spacing of 100 nm.

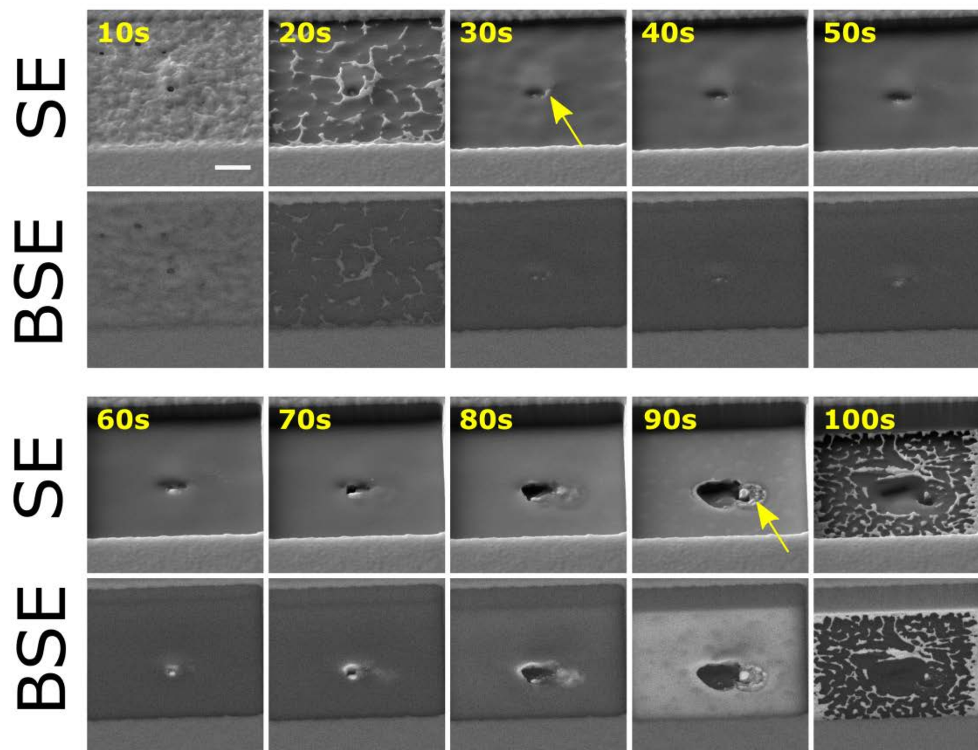

Figure 4 Top-down milling of the conductive filament as a function of the eplased time (10 s-100 s), where the scale bar represents 1 μm and the cross-sectional image of the conductive filament was taken from the location of the yellow arrow.

As discussed in Figure 2, Joule heat plays an important role in the determination of I–V curves, in which current fluctuations also occur throughout the SET and RESET processes. FIB milling of the Cu/Cu-doped SiO_2/W device was performed via Ga ions using a dual-beam scanning electron microscope (DBEM) (Tescan, LYRA3) at a 30 kV acceleration voltage with an emission current of 2 μA and a beam current of 12 nA. The top-down milling of the device proceeded in places with defects, such as particles and voids, as exhibited in Figure 4. After 30 s of milling, the topmost Cu electrode was completely removed. The particles with heavier elements (light white in BSE mode) were present throughout the milling process (marked with yellow arrows), suggesting the existence of metallic filaments. In other words, successive cross-sectional images of conductive filaments were captured to construct a 3D model of conductive filaments. After 100 s of milling, the bottom tungsten electrode was almost depleted, which was

further confirmed by the EDS spectra shown in Figure S2 (b)-(c). The formation of pores is attributed to the weakened structure of the material caused by the conductive filaments, which are prone to severe etching.

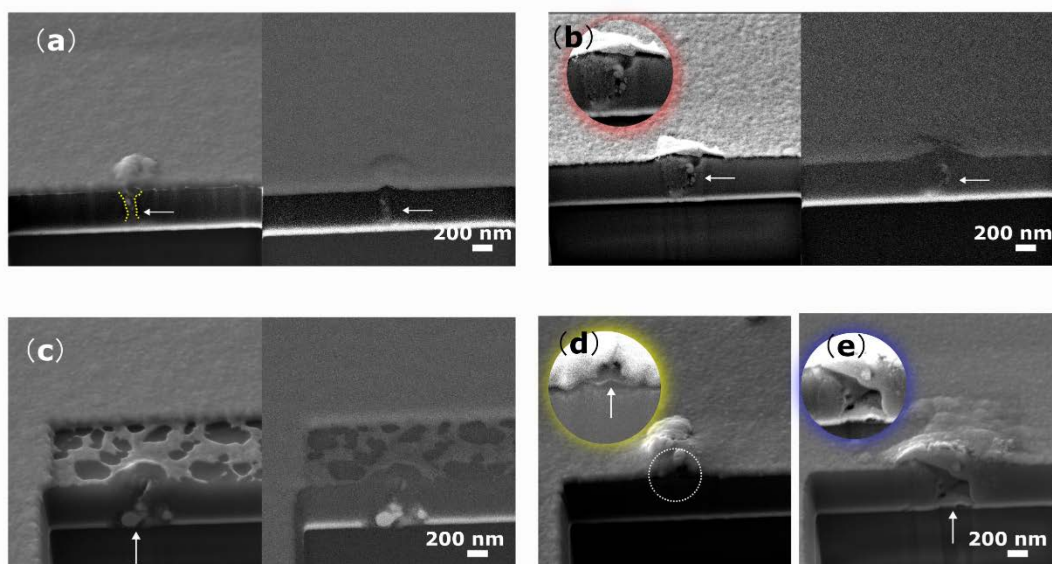

Figure 5 (a) SEM image of a conductive filament in an SE (left) and a BSE (right), marked by the yellow dashed line and arrow, which bridge the top and bottom electrodes; (b) the partially ruptured conductive filament in an SE (left) and a BSE (right), and the inset shows an enlarged image from the place of a white arrow; (c) the nanosized particles derived from a conductive filament in an SE (left) and a BSE (right); (d) the delaminated single layer from 2D SiO_2, where the inset shows the enlarged image of exfoliated layers from the dashed circle; (e) the void generated from the evaporation of a conductive filament, where the inset shows the enlarged image of the void.

Since the location of the conductive filament is randomly distributed throughout the electrodes, a sideview of the conductive filament was obtained in a Cu/Cu-doped SiO_2/W device (SET state) employing back-forward FIB milling. The intervals between each cross-sectional image were controlled at 100 nm, and all series of images are presented in the supplementary material (Figures S3-S7). Since the thickness of the Cu-doped SiO_2 layer is approximately 500 nm (as shown in Figure S3), heavy copper doping was employed to increase the ionic conductivity of the electrolyte layer and facilitate the formation of conductive filaments. Due to the random distribution of conductive filaments, FIB milling was performed in regions with particles, which possibly consisted of conductive filaments. An intact conductive filament joining the topmost and bottom electrodes was observed in the device in the SET state, as shown in Figure 5 (a). The lighter white shade in the BSE image further confirms the existence

of conductive filaments at the location of the white arrow. Before FIB milling, two particles were clearly deposited on the surface of the electrode. With the continuation of milling, the conductive filament, close to the top electrode, appeared, as shown in Figure S3 (e). From Figure S3 (f) to Figure S3 (g), the conductive filament extended gradually to the bottom electrode. The rest of Figure 5 (b)-(e) were taken from the Cu/Cu-doped SiO_2/W in the RESET state. In the device in the RESET state (Figure 5(b)), an inconsistent conductive filament was found beneath the surface particles, which comprised a series of nanoparticles. Furthermore, due to the vaporization of the conductive filament, Cu electrode was detached from the underlying electrolyte, revealing a visible gap. As a result, the filament at this spot could not be rebuilt in the following SET cycle. As shown in Figure S4, before milling, one particle with pores was present. The detachment of the topmost electrode from the underlying Cu-doped SiO_2 was observed throughout the entire milling process, and the inconsistent conductive filament is presented in Figure S4 (h) to Figure S4 (j), where the metallic nanoparticles are clearly visible in Figure S4 (i).

Generally, metallic particles with diameters of 100-200 nm, which were possibly melted within conductive filaments, were also observed in the device in the RESET state. As shown in Figure S5 (f) and (g), the metallic particles were deposited close to the Cu electrode, which suggested that the conductive filament was dissolved in the vicinity region of the topmost copper electrode. In addition to the meltdown of conductive filaments, the vaporization of conductive filaments under high current density was also observed with the morphology of defects, including the exfoliation of 2D SiO_2 and microcavities. As shown in Figure 4 (d), the vapor exfoliated adjacent single layers of SiO_2, thus detaching the underlying layers from the topmost electrode. A long crack appeared during the milling of the device, as shown in Figure S6 (j)-(l). Furthermore, a large quantity of vapor can trigger even more damage. As shown in Figure 4 (e), the vapor formed a giant cavity that connected the top and bottom electrodes. The depth of the cavity, presented in Figure S7 (j)-(n), suggested that vaporization of the Cu electrode could occur, demonstrating strong Joule heat during the DC sweep.

In summary, although the SEM images were captured at the same time intervals during top-down milling, the sputtering rates were different throughout the surface of the sample due to defects. Therefore, 3D modeling of conductive filaments is rather imprecise than that of front-back milling. Furthermore, the drifts of the sample caused by local heating by the electron beam also affect the milling of the devices and the quality of the images, especially for long-term milling; thus, milling and imaging in short time intervals would be better for improving the quality of 3D models.

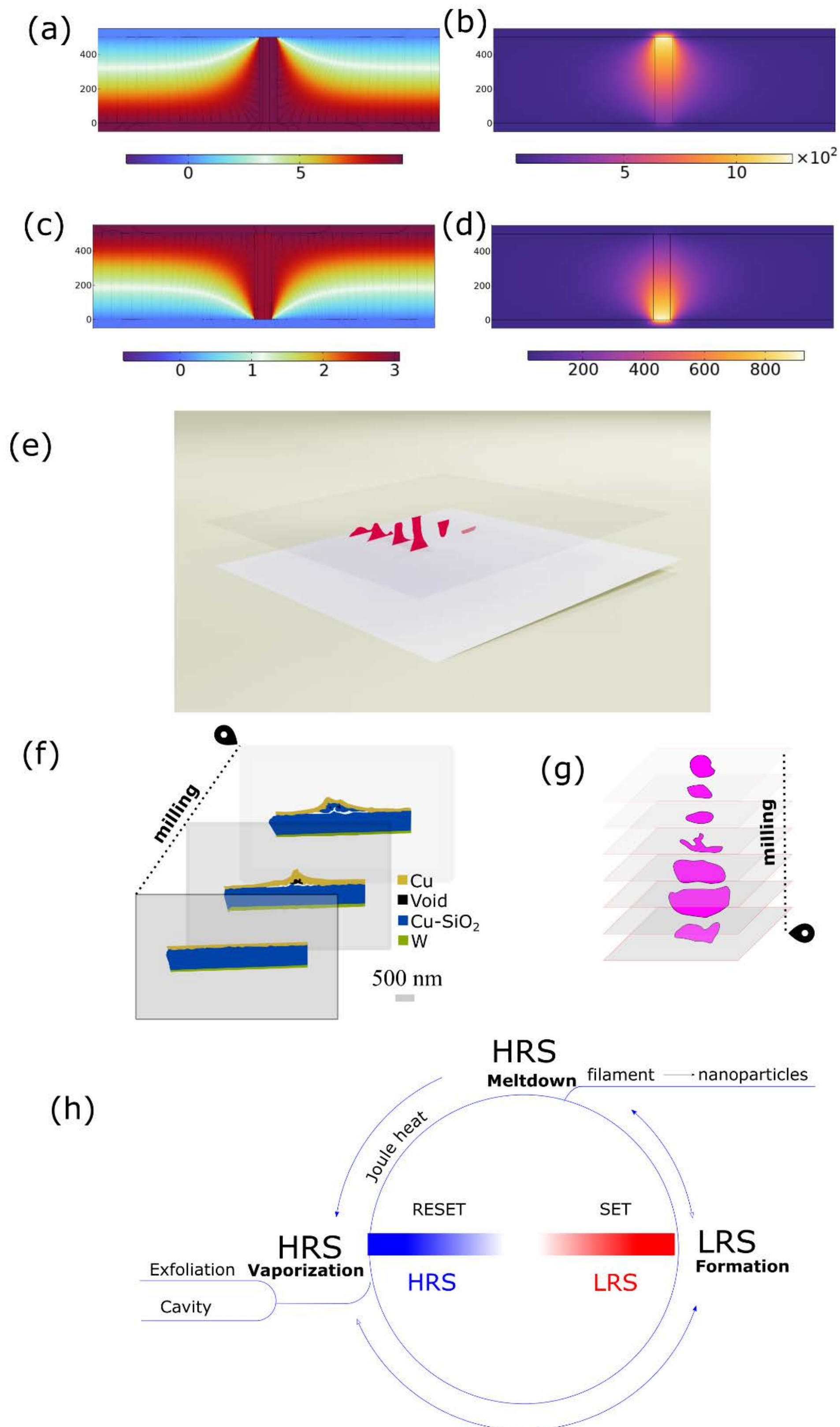

Figure 6 (a) Voltage distribution at a -9.5 V bias; (b) temperature distribution (in deg C) at a -9.5 V bias; (c) voltage distribution at a 3 V bias; (d) temperature distribution (in degC) for a 3 V bias; (d) 3D construction of conductive filaments achieved by front-

back milling; (d) 3D construction of defects, where the legend of defects is shown at the right corner; (d) 3D construction of conductive filaments by top-down milling; and (d) mechanism of resistance change involving vaporization, meltdown and formation of conductive filaments.

The distributions of temperature and electric voltages were simulated via COMSOL using AC/DC and Heat Transfer module. The following time dependent Heat Transfer equation was used for numerical simulation:

$$\rho c_p \frac{\partial T}{\partial t} - \nabla \cdot (\kappa \nabla T) = Q_e$$

where $Q_e = \vec{J} \cdot \vec{E}$ is ohmic heating due to electric current with current density $\vec{J}$ and electric field strength $\vec{E}$, and c_p, ρ and κ are heat capacity, density, and thermal conductivity of material.

Since the DC sweep was conducted in air, the oxidation of Cu and W electrodes should be considered; thus, thin CuO and WO_3 layers were added to the model, and their thicknesses were determined as follows. In Fig. S8, the influence of the thicknesses of the CuO and WO_3 layers on the maximal temperature within the device calculated via COMSOL is shown. In the RESET state, the main influence on the maximal temperature was the CuO layer, which WO_3 layer had an almost negligible influence (see Fig. S8 (b)). On the other hand, in the SET state, one can also observe the influence of the WO_3 layer (see Fig. S8 (a)). The resulting thicknesses of CuO and WO_3 are 3 nm and 0.2 nm, respectively. As shown in Figure 6 (a)-(d), we set the diameter of the conductive filament to 100 nm, which is in agreement with the SEM images. In the RESET process, the temperature of the filament exceeds 1200 °C at -9.5 V, which is higher than the melting temperature of Cu (1085 °C). During the SET process, the temperature exceeded 930 °C at 3 V, which confirmed the melting or vaporization of the conductive filaments, as described in the previous text. The properties of materials used in the simulation are summarized in Table S1. A 3D model of the conductive filament was obtained via front-back milling, as shown in Figure S3 (f)-(g), where cross-sectional images of the conductive filaments are presented in Figure 6 (e). As demonstrated in Figure 5 (a), the conductive filament joined the topmost and bottom electrodes in 2D mode. Nevertheless, from the 3D views, the position of the conductive filament was slightly tilted, and such a complex morphology can be found only when employing the FIB milling method. As exhibited in Figure S8, the cross-sectional images are plotted from successive SEM images presenting the 3D model of defects. Due to the vaporization of the conductive filament, the adjacent single layers were delaminated, resulting in a permeant high-resistance state, as shown in Figure 6 (f). The detailed 3D construction of conductive filaments is presented in Figure S9, where a gap gradually developed into a giant crack from Figure S9 (1)-(11). The 3D model of a single conductive filament can also be estimated from top-down FIB milling, as shown

in Figure 6 (g). In the future, the 3D model can be further improved by introducing smaller time intervals, hence enabling a smooth transition between each figure.

In the classic ECM model, the formation and dissolution of conductive filaments are attributed to nondestructive operation, where cyclic DC sweeps do not influence memristive devices. According to our experimental results, the vaporization of conductive filaments, which is driven by Joule heat, should be an important missing part of the ECM model. As shown in Figure 6 (h), we suggest a model with 3 factors, in which the formation, meltdown, and vaporization of the conductive filament contribute to the resistance switches. During the positive DC sweep, ions are reduced into a conductive filament joining the topmost and bottom electrodes in a low-resistance state (LRS). As a consequence, the current ramps up dramatically, resulting in a substantial amount of Joule heat. Therefore, the newly formed conductive filaments can be melted down or vaporized, which results in a high-resistance state (HRS). In this situation, both the LRS and HRS are in a metastable state, reflecting a fluctuation in the current in the I-V curve. Moreover, a similar situation also occurs in the RESET state, which does not simply switch the device into an HRS. From the view of morphologies, we can also find solid evidence supporting our model. First, the vaporization of conductive filaments generally causes a series of defects, especially voids or cracks. In some other cases, the particles were present, whereas the voids or cracks were hidden. As shown in Figure 4, we found an intact conductive filament from the device in the SET state and a ruptured conductive filament in the RESET state. Once the filament is fully melted and cannot be dissolved back to the SiO_2 matrix, large metallic particles are formed. When a particle is vaporized, enormous pressure is applied to the SiO_2 matrix, resulting in cracks or voids.

Conclusion

In this paper, we found solid evidence from the SEM images of devices after DC sweeps, in which defects of particles, bubbles, cavities, and voids were found. To determine the morphology or structure under these defects, we milled the surface electrode of the device with an FIB along the front-back and top-bottom directions to remove the surface material; thus, 3D construction of defects and conductive filaments was accomplished. FIB-SEM images further revealed that the vapor exfoliated adjacent single layers of $SiO_{2,}$ resulting in permanent damage to the memristive device. The simulation of the temperature and voltage gradient supports the vaporization of the conductive filament, in which the temperature of the conductive filament exceeds the melting point of Cu. From the I-V curve, the vaporization of the conductive filament can also be seen as a fluctuation in the current during the I-V measurement.

In summary, without applying an external bias, the resistance of the memristive device was initially high. With increasing positive bias, the ions migrated and were reduced to form a conductive filament. Moreover, the current ramped up, causing the generation of Joule heat concentrated around the conductive filaments. Afterwards, the conductive filaments were vaporized to exfoliate adjacent single layers and expand the internal

voids or large cavities inside the electrolyte layer. A similar process also occurred in the RESET process since it did not provide protection from the compliance current. Therefore, in both the SET and RESET processes, the resistance of the device was always unstable, resulting in fluctuations in the current. Our model enriches the traditional ECM model with a new definition and concept, which helps to improve the performance of memristive devices. In the future, methods should also be explored to reduce the damage to memristive devices caused by Joule heating, which improves the lifetime of memristive devices.

Experiment

The devices were prepared using RF sputtering. This led to the deposition of 2D Cu-doped SiO_2 onto the silicon wafer by means of a combination of Cu and SiO_2 targets, which is referred to as a “composite target”. The RF sputtering configuration is shown in Figure S1. The composition of the Cu-doped SiO_2 was regulated by the size of the opening of the aperture and the RF power. Exfoliation of the Cu-doped SiO_2 was completed using treatment with a saturated $FeCl_3$ acetone solution. Then, the samples were rinsed with distilled water many times and transferred to an optical microscope for observation. The details of the surface morphology were also examined using an SEM S4800 at an acceleration voltage of 10 kV. The height of the steps and topographical image were studied by means of an AFM (atomic force microscope) (Veeco). X-ray photoelectron spectroscopy (XPS) was conducted using a Thermo Scientific^{TM} K-Alpha spectrometer equipped with a monochromatic Al Kα X-ray source (1486.6 eV) operated at 100 W. The samples were analyzed under vacuum ($P < 10^{-8}$ mbar) with a pass energy of 150 eV (survey scans) or 25 eV (high-resolution scans). All the XPS peaks were calibrated for adventitious carbon with a C1s peak binding energy of 284.8 eV. The experimental XPS peaks were fitted using Avantage software. The crystalline structure of the materials was characterized via X-ray diffraction (XRD) (Rigaku) using Cu Kα radiation (λ=0.1542 nm).

The devices were fabricated in a classic crossbar configuration with 3 layers (W (bottom)/2D Cu-doped SiO_2/Cu (topmost)). The size of the cross point was 100 μm × 100 μm. Subsequent DC sweeps were measured using a Keithley 2600 multimeter equipped with probes, where the positive electrode was connected to the topmost Cu electrode and the negative electrode was connected to the bottom electrode. In addition to the normal DC sweep measurements, one type of device was set to a high-resistance state, while the other samples were set to a low-resistance state for further FIB milling. After the DC sweep had been measured, all the samples were studied via SEM imaging. The electrical field and heat distribution of the devices were simulated by means of COMSOL software using the Poole-Frenkel/Schottky dependence model for the CuO and WO_3 layers: $\sigma = \sigma_0 \cdot exp\left(\sqrt{\frac{eV}{kT}}\right)$. Ga ion milling of the sample was carried out using a dual beam scanning electron microscope (DBEM) (Tescan, LYRA3), and FIB

was performed at a 30 kV acceleration voltage with an emission current of 2 μA and a beam current of 12 nA. Two types of milling were used: front-back and top-bottom milling. The top-bottom milling was stopped every 10 seconds, during which the SEM scans were obtained at an acceleration voltage of 10 kV in the FIB-sputtered areas.

ACKNOWLEDGMENT

The author thanks for financial support from the grant of the Ministry of Education,

Youth- and Sports of Czech Republic (grant LM2023037), , the European Regional

Development Fund Project, the project NANOMAT

CZ.02.1.01/0.0/0.0/17_048/0007376 and the project of Faculty of Chemical

Technology, University of Pardubice "Excellent teams" 2023， the grant of Hebei

Normal University (L2021B12) and the HeBei NSF (QN2023054)

REFERENCE

1 Y. Hirose and H. Hirose, *J Appl Phys*, 1976, 47, 2767–2772.
2 R. Waser and M. Aono, *Nat Mater*, 2007, **6**, 833–840.
3 A. Gubicza, D. Zs. Manrique, L. Pósa, C. J. Lambert, G. Mihály, M. Csontos and A. Halbritter, *Sci Rep*, 2016, **6**, 30775.
4 F. Longnos, E. Vianello and C. Carlo, *Solid State Electron*, 2013, **84**, 155–159.
5 S. Bera, A. K. Katiyar, A. K. Sinha, S. P. Mondal and S. K. Ray, *Mater Des*, 2016, **101**, 197–203.
6 J. Van Den Hurk, I. Valov and R. Waser, *Thin Solid Films*, 2013, **527**, 299–302.
7 X. Guo, C. Schindler, S. Menzel and R. Waser, *Appl Phys Lett*, 2007, **91**, 133513.
8 C. Schindler, Technischen Hochschule Aachen, 2009.
9 J. Joshua Yang, F. Miao, M. D. Pickett, D. A. Ohlberg, D. R. Stewart, C. N. Lau and R. S. Williams, *Nanotechnology*, 2009, **20**, 215201.
10 Y. Yang, P. Gao, S. Gaba, T. Chang, X. Pan and W. Lu, *Nat Commun*, 2012, 3, 732.
11 C. Chang, J. Chen, C. Huang, C. Chiu, T. Lin, P. Yeh and W. Wu, *Small*, 2017, **13**, 1603116.
12 C. Sang Jun, P. Gyeong Su, K. Ki Hong and C. Soohaeng, *Advanced Materials*, 2011, **23**, 3272–3277.

13 Q. Liu, J. Sun, H. Lv, S. Long, K. Yin, N. Wan, Y. Li, L. Sun and M. Liu, *Advanced Materials*, 2012, **24**, 1844–1849.

14 Y. Li, M. Zhang, S. Long, J. Teng, Q. Liu, H. Lv, E. Miranda, J. Suñé and M. Liu, *Sci Rep*, 2017, **7**, 11204.

15 K. Min, D. Jung and Y. Kwon, *Sci Rep*, 2021, **11**, 2447.

16 S. M. Hus, R. Ge, P.-A. Chen, L. Liang, G. E. Donnelly, W. Ko, F. Huang, M.-H. Chiang, A.-P. Li and D. Akinwande, *Nat Nanotechnol*, 2021, **16**, 58–62.

17 X. Xia, W. Huang, P. Hang, T. Guo, Y. Yan, J. Yang, D. Yang, X. Yu and X. Li, *ACS Mater Lett*, 2023, **5**, 1109–1135.

18 P. Kumbhakar, C. Chowde Gowda, P. L. Mahapatra, M. Mukherjee, K. D. Malviya, M. Chaker, A. Chandra, B. Lahiri, P. M. Ajayan, D. Jariwala, A. Singh and C. S. Tiwary, *Materials Today*, 2021, **45**, 142–168.

19 B. Zhang, V. Cicmancova, B. Ludvik, S. Slang, P. Kutalek, M. Motola and T. Wagner, *Adv Mater Interfaces*, 2022, **9**, 2201790.

20 C. Schindler, S. Chandran Puthen Thermadam, R. Waser and M. N. Kozicki, *IEEE T-ED*, 2007, **54**, 2762–2768.